South-Pole Aitkin Basin Ejecta Reveal the Moon's Upper Mantle

SUPPLEMENTAL MATERIAL:

DATA AVAILABILITY:

Final Figures and Tables will be archived on Purdue's PURR data archive system. The iSALE computer code is available upon request from developers Garth Collins or Kai Wünnemann (www.isale-code.de). The simulation results are available upon request from Jordan Kendall (jordan.d.kendall@gmail.com).

HYDROCODE MODELING

We simulate the impact crater and ejecta formation (Supplementary Figure DR1) with the iSALE-3D shock physics code (Wünnemann et al., 2006; Collins et al., 2004; Elbeshausen et al., 2009; Elbeshausen and Wünnemann, 2011). The iSALE-3D code uses an Arbitrary Lagrangian-Eulerian formulation (Hirt et al., 1974). Previous studies validated the iSALE code against comparable hydrocodes, cratering observations, and laboratory experiments (Pierazzo et al., 2008; Davison et al., 2011; Elbeshausen and Wünnemann, 2011)

Our model Moon consists of a 680 km diameter iron core overlain by a 1400 km thick dunite mantle with a surface gravity of 1.618 m/s^2 (Supplemental Table DR1). Dunite has a similar composition as the Moon's bulk mantle and the equation of state is well defined within the iSALE ANEOS library (Benz et al., 1989; Pierazzo et al., 1997). We model the Moon's iron core with the ANEOS tabular data for iron (Thompson, 1990). We infer that if a 15 km/s impact velocity will eject upper mantle material, then higher velocities will as well. We vary impact angle, between 30° and 60°, and impactor diameter, between 200 and 420 km (Table 1 and Supplemental Table DR1). This range of impact scenarios is in agreement with previous studies of the SP-A basin transient crater diameter (Potter et al., 2012). The model uses a pressure and damage dependent strength model, developed for rock-like materials (Collins et al., 2004), for dunite and a strain and strain-

33   rate dependent strength model for metals (Johnson and Cook, 1983) for the Moon's iron

34   core (Supplemental Table DR2). The SPA-forming impact deposited a large amount of

35   mantle material on the farside highlands of the moon, with an increasing concentration of

36   crustal material at greater ranges.

37

38   It would have been more accurate to model the Moon's upper mantle as orthopyroxene

39   for these simulations, but a shock equation of state for this material does not exist. The

40   Hugoniot curves for forsterite and enstatite, however, are similar (Marsh 1980), so our

41   use of dunite does not affect our conclusions. Similarly, we use dunite for the impactor

42   only out of convenience: Crater excavation depends almost entirely on the mass and

43   energy delivered by the impactor, not its composition. A mineralogically distinct crust is

44   not included in these models, although a stiff mechanical surface layer is enforced by the

45   initial temperature distribution, with a near-surface thermal gradient of 10 K/km,

46   following the low value in Potter et al. 2012. This gradient may be too small for the time

47   of the SPA impact (Laneuville et al., 2013) assume 17.5 K/km at 4 Gyr), but the thermal

48   gradient has only a small effect on the transient (although not the final, collapsed) crater

49   (Potter et al. 2012).

50

51   We assumed a crustal thickness of 50 km. This is on the thick side of the Wieczoreek et

52   al. 2012, crustal models, but our 10 km resolution forces a choice of either 40 or 50 km

53   and we made the conservative choice.

54

55   We place Lagrangian tracers, which track the motion of a parcel of material through the

56   Eulerian mesh, in the center of each cell of the simulation space (Supplemental Table

57   DR1). We treat these tracers as proxies for the ejected mass from the impact, with each

58   tracer representing a volume of 1000 km^3 (determined by the resolution of the simulation).

59   We track the tracer trajectories and determine the locations where they ballistically

60   emplace on the lunar surface relative to the current location of the SP-A basin (Figures 1,

61   2, and DR2).

62

63   The impact ejects Lagrangian tracer particles out of the opening transient crater. As the

64   tracers pass through an altitude 40 km above the initial surface of the Moon, we

65   determine if the tracers are ballistic from each tracer's position, $\vec{x}_i$, and velocity, $\vec{v}_i$,

66   relative to the Moon's frame of reference. We determine the escape velocity at each

67   tracer's position, $\vec{v}_{i,esc} = \sqrt{2GM/|\vec{x}_i|}$, where $M = 7.348 \cdot 10^{22} kg$ is the mass of the

68   Moon, $G = 6.67384 \cdot 10^{-11}\ m^3 s^2 / kg$ is the gravitational constant. If the magnitude of

69   the tracer velocity is below escape velocity, $|\vec{v}_i| < |\vec{v}_{i,esc}|$, we extrapolate a ballistic

70   trajectory and impact point by determining the ballistic range and direction along the

71   spherical Moon's surface.

72

73   We use the emplaced tracer positions to create a map of ejecta thickness (Figure 1),

74   excluding any tracers that land within the transient crater diameter, inside of which crater

75   collapse occurs (Melosh, 1989). We report the transient crater diameters, maximum depth

76   of ejecta provenance, and volume of ejecta (Table 1). We place the emplaced tracer

77   positions into equal surface area bins along the lunar surface. The longitude and the sine

78   of the colatitude allow equal-area bins along the surface of the Moon. We calculate the

79   ejecta thickness in each bin by dividing the volume of ejecta by the surface area of each

80   equal-area bin. In order to calculate the volume of ejecta, we use the initial density of

81   each cell at t=0 s which varies with depth, as determined by hydrostatic equilibrium.

82   Then, we use the initial density to calculate a mass for each tracer and the final volume,

83   assuming a density (Wieczorek et al., 2013) of 2650 kg/m³. Next, we plot the results in

84   latitude and longitude so that the SP-A basin is centered at -53.2° latitude and 191°E

85   longitude (Garrick-Bethell and Zuber, 2009) (Figure 1). Assuming a final density is

86   uncertain because the impact ejects large volumes of mantle material and we may be

87   overestimating the final volume by assuming a density of 2650 kg/m³. Retaining a density

88   of 3200 kg/m³ more appropriate for pure mantle material would decrease our estimates by

89   ~20%.

90

91   In addition to the results shown in Figure 2, we include two more bar plots of ejecta

92   thickness along radial lines; in the direction of 0° and 90° from the direction of the

93   impact (Supplemental Figure DR2). We mark these lines in Figure 1 as the solid and

94   dashed red lines respectively.

95

96   **Supplemental Table DR1:** iSALE-3D model description (Chicxulub release)
97

Parameter description	Value
Number of high resolution cells in x-direction	450
Number of high resolution cells in y-direction	250
Number of high resolution cells in z-direction	450
Cell size	10 km
Physical dimension of entire mesh, x-direction	-2700 km to +1800 km (horizontal)
Physical dimension of entire mesh, y-direction	0 to +2500 km (into plane of impact)
Physical dimension of entire mesh, z-direction	-1800 km to +2700 km (vertical)
Surface Temperature	300 K
Surface gravitational acceleration	1.618 m/s^2
Projectile Diameter	200 to 420 km
Impact Velocity	15 km/s
Target Mantle Radius	1740 km
Target Core Radius	350 km

98

99 **Supplemental Table DR2:** iSALE-3D material input parameters (Chicxulub release)

100

Description	Values for Dunite	Values for Iron
Equation of State	ANEOS Dunite [a]	ANEOS Iron [b]
Melting Temperature	1373 K	1811 K
Specific Heat	1300	600
Poisson's ratio	0.25	0.25
Thermal Softening Model	Ohnaka (1995)	Ohnaka (1995)
Thermal Softening Parameter[c]	1.1	1.2
Simon A parameter[c]	1520 MPa	6000 MPa
Simon B parameter[c]	4.05	3.00
Cohesion (undamaged)[d]	5.07 MPa	0
Cohesion (damaged)[d]	0.01 MPa	0.01 MPa
Frictional Coeff. (undamaged)[d]	1.58	0
Frictional Coeff. (damaged)[d]	0.63	0.4
Strength at Infinite Pressure[d]	3.26 GPa	2.50 GPa
Strain Coefficient, a*	N/A	3.24E+08
Strain Coefficient, b*	N/A	1.14E+08
Strain Exponent, n*	N/A	0.42
Strain rate coefficient, c*	N/A	0
Pressure coefficient, d*	N/A	0
Minimum Pressure*	N/A	0 Pa
Porosity Model	None	None

101 [a]See Benz et al. (Benz et al., 1989). [b] See Thompson et al. (Thompson, 1990) [c]See

102 Wünnemann et al. (Wünnemann et al., 2006) and Ohnaka (Ohnaka, 1995) for a thermal

103 softening model description within iSALE. [d]See Collins et al. (Collins et al., 2004), for

104 the pressure and damage dependent strength model description within iSALE. *See

105 Johnson and Cook (Johnson and Cook, 1983) for a strain and strain-rate dependent

106 strength model developed for metals.

107

**a)** t = 0 s   **b)** t = 300 s   **c)** t = 1000 s
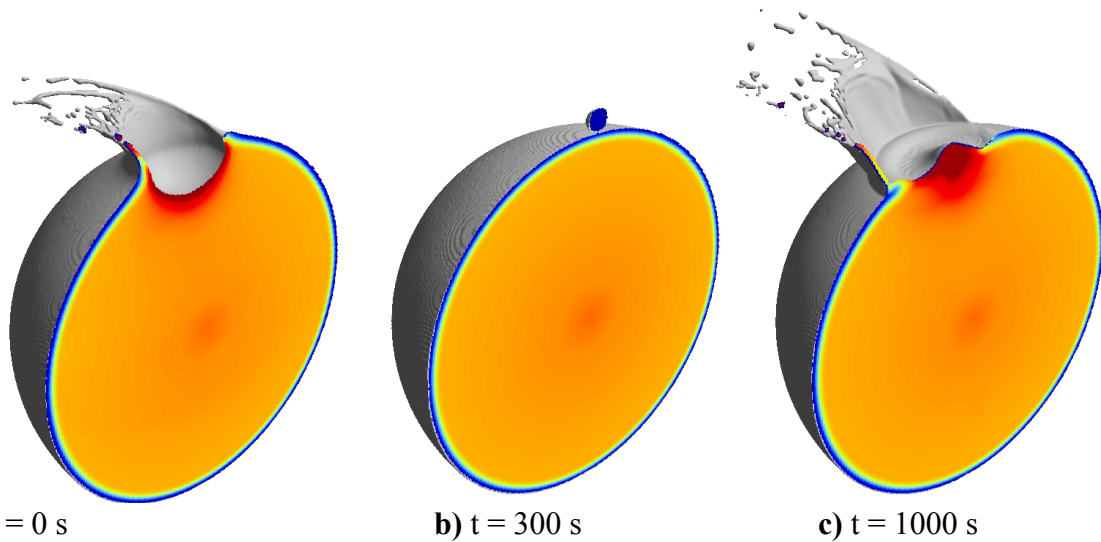
Supplemental Figure DR1: Before impact, transient crater formation, and crater collapse of an impact of a 200 km diameter impactor striking a 1740 km radius Moon with a 15 km/s impact velocity in iSALE-3D. The impact angle is 45° from the horizon. An isosurface (dark grey) represents the interface between the surface and vacuum (white region) and a temperature cross-section shows values from 300 K (blue) to >1900 K (red).
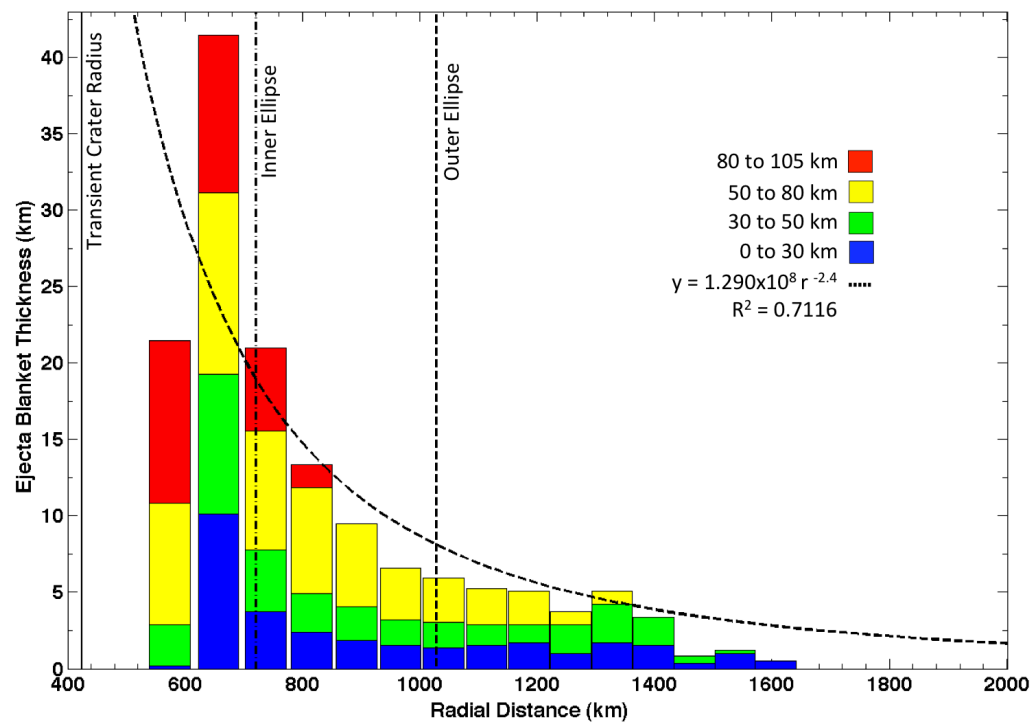
Figure DR1 Animation

2017360_Fig DR1 Animation.gif

118

119   a.)

120

121   b.)

122
123
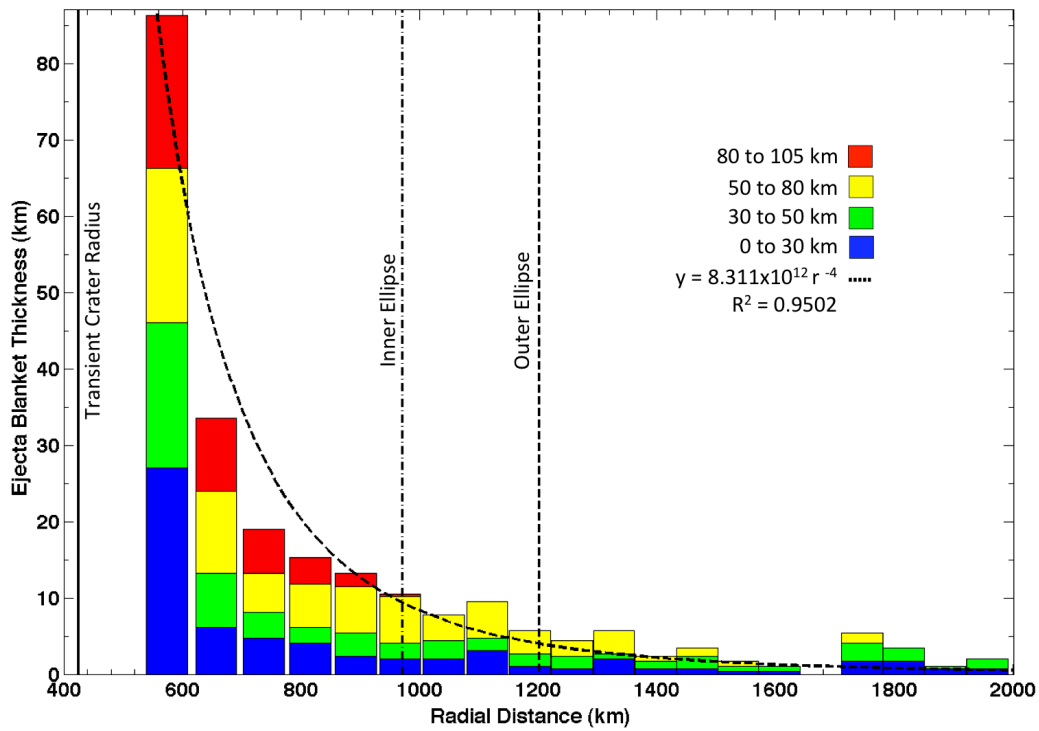
124   **Supplemental Figure DR2:** Ejecta thickness as a function of depth of origin along a

125   radial line from the basin center, plotted along a line a.) 0° and b.) 90° to the impact

126   direction (solid and dash red line in Figure 1 respectively) for the nominal 200 km

127   diameter projectile striking at 45° to the surface. Because deeper-seated ejecta land later

128   than shallower material, the stratigraphy is inverted, although mixing may occur due to

129   the higher impact velocity at large ranges. The vertical lines correspond to the crater rim

130   and the dashed circles plotted in Figure 1. The light dashed line is a best fit of the ejecta

131   thickness to a $1/r^N$ dependence of ejecta thickness on range. The large deviation at the

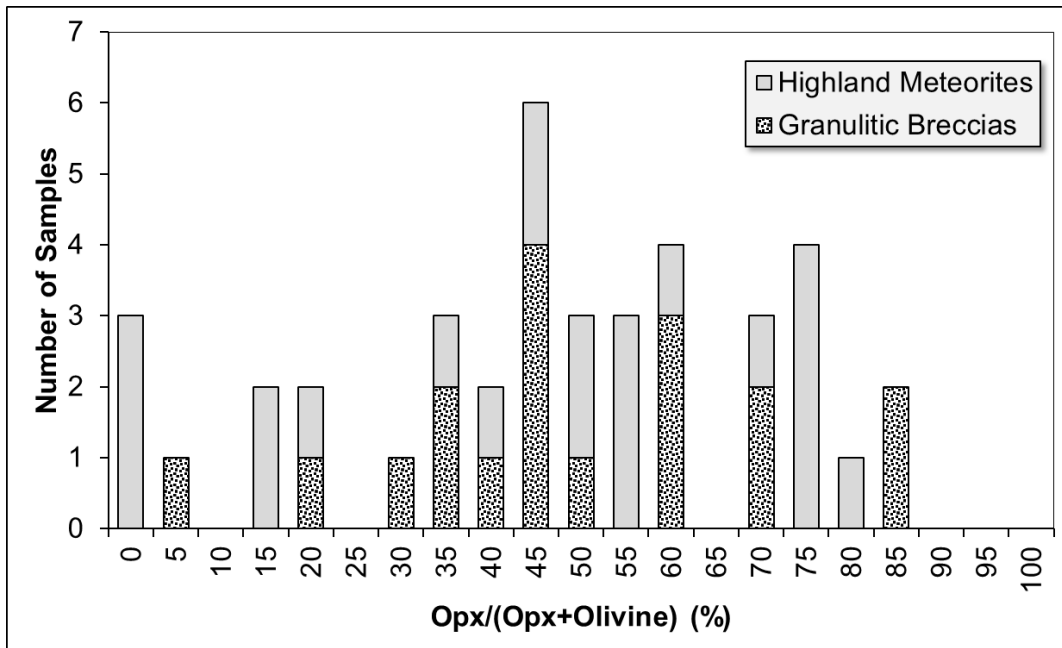132   crater rim will be quickly reduced as the transient crater collapses.

133

134   **ORTHOPYROXENE AND OLIVINE IN HIGHLAND SAMPLES**

135   Two suites of highland samples have mineral abundances consistent with

136   substantial amounts of low-Ca pyroxene in their mafic assemblages. One is a texturally

137   and compositionally diverse group of breccias called the granulitic suite, which were

138   thermally metamorphosed in large craters (Cushing et al. 1999; Hudgins et al. 2011). The

139   granulitic suite shows distinctive correlations between mg# and increasing olivine/LCP

140   (Fig. DR3) and decreasing plagioclase (not shown), suggesting that the rocks are

141   mixtures of a mafic component with ferroan anorthosite. The data do not allow

142   unambiguous identification of the mafic component (cumulate intrusive rocks such as

143   troctolites and norites, or mantle rocks with varying LCP/olivine). Nevertheless, the data

144   show that the granulitic suite contains substantial amounts of LCP. Normative mineral

145   abundances in meteorites from the lunar highlands also indicate abundant LCP among the

146   mafic minerals in the highlands (Fig. DR4). If the olivine-LCP component reflects the

147   composition of the lunar mantle, then the mantle contains on average substantial amounts

148   of both LCP and olivine.

149

150
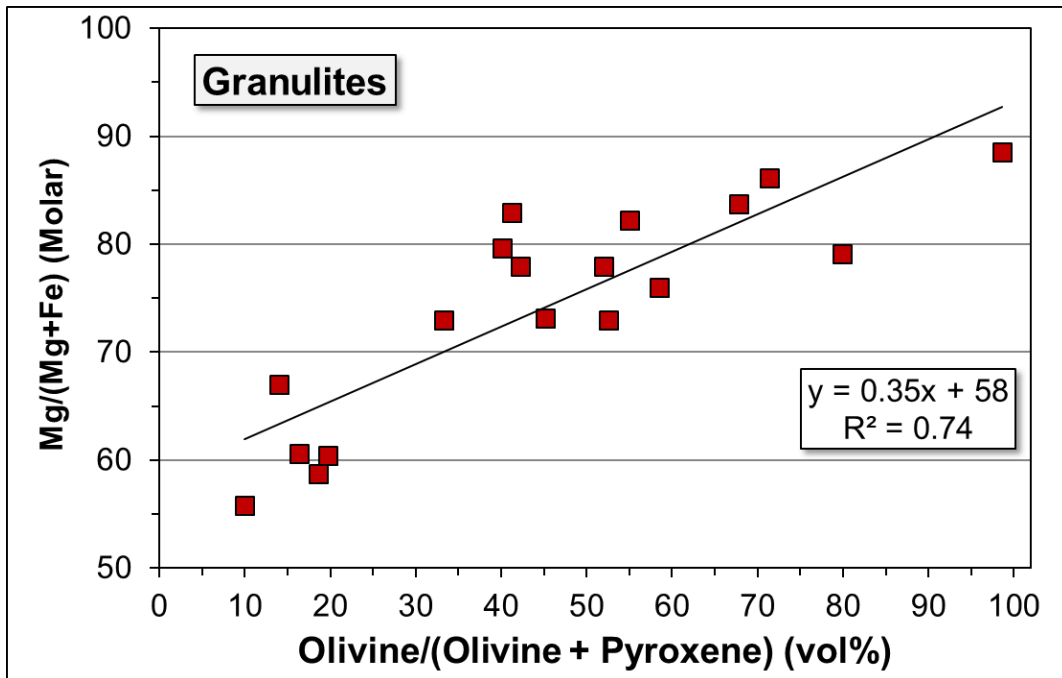
151 **Supplemental Figure DR3:** Modal olivine abundance (vol%) among all mafic silicates

152 (olivine + Low-Ca Pyroxene + High-Ca Pyroxene) versus Mg#. The data fall along a

153 linear trend suggesting that granulitic breccias are mixtures of ferroan anorthosites (low

154 Mg#) with mafic rocks that vary in Mg# and olivine/orthopyroxene. Data from numerous

155 sources in the literature.

156

157

158   **Supplemental Figure DR4:** Frequency distribution of modal (granulitic breccias) and

159   normative (lunar highland meteorites) of orthopyroxene (Opx) compared to the total

160   olivine and orthopyroxene assemblage. The relative abundances of olivine and

161   orthopyroxene vary widely, but over half of the samples in both groups of lunar samples

162   contain more orthopyroxene than olivine. Data from numerous sources in the literature.

163

164

165   **SPECTRAL ANALYSIS**

166   We used visible/near-infrared spectral data (0.43-3μm) from the Moon

167   Mineralogy Mapper (M³) imaging spectrometer(Pieters et al., 2009; Green et al., 2011)

168   (M³) on Chandrayaan-1 to characterize the iron-bearing minerals associated with SPA

169   and surrounding terrains. M³ Level 2 reflectance data from the global mapping campaign

170   was acquired from the Planetary Data System, which includes corrections for thermal

171   emission as well as topographic, photometric, and instrumental effects (Green et al.,

172   2011; Clark et al., 2011; Hicks et al., 2011; Boardman et al., 2011; Besse et al., 2013).

173   Our mosaics include 28 images (Supplemental Table DR3), all from the "2A" period of

174   mission operations (April 15-27, 2009) with 140 m/pixel resolution.

175   VNIR spectral analysis cannot differentiate between pigeonite and a physical

176   mixture of clinopyroxene and pure orthopyroxene. The average 1 μm band centers over

177   the entire mapped region are close to 0.95 μm, which based on the results of Cloutis and

178   Gaffey (1991), this implies that the bulk ejecta could contain up to 10-15% wollastonite

179   or clinopyroxene. However, the strongest LCP signatures exhibit band centers closer to

180   0.92 μm, consistent with very little (0-10%) wollastonite (e.g., Supplementary Figure

181   DR5). In addition, the low band center and symmetric shape of 1 μm bands in the ejecta

182   suggests little to no olivine contribution (Horgan et al., 2014)

183   To extract information on iron mineralogy from the spectra, the overall continuum

184   slope must be suppressed by removing an approximate continuum function using the

185   linear convex hull method (Bennett et al., 2016). To find the continuum function, we first

186   smooth each spectrum with nested boxcar average and median smoothing functions, both

187   3 channels wide. Then, we remove an initial estimate of the continuum, fit to fixed

188   endpoints at 0.7, 1.5, and 2.6 μm. Next, we fine-tune these endpoints for each spectrum

189   by finding the local maxima in this initial continuum removed spectrum. For the 1 μm

190   region, we find the local maxima between 0.6-1.0 and 1.0-1.7 µm, which become the new

191   endpoints. For the 2 µm region, local maxima are found between the previous endpoint

192   (between 1.0-1.7 µm) and 2.0 µm and 2.0-2.6 µm. These ranges avoid both possible long-

193   wavelength plagioclase absorptions near 1.3 µm and thermal effects beyond 2.6 µm.

194   Using the new endpoints, the final continuum of three joined linear segments is

195   calculated from the original spectrum.

196   Iron-bearing minerals can be identified in M^3 data based on the position and shape

197   of the 1 and 2 µm iron absorption bands, which vary significantly with mineralogy and

198   composition(Adams, 1974; Cloutis and Gaffey, 1991; Sunshine and Pieters, 1993;

199   Horgan et al., 2014). We use the methods of Horgan *et al*. (Horgan et al., 2014) to map

200   the position of the 1 and 2 µm iron absorption bands, which are indicators of iron

201   mineralogy. Band position is parameterized as band center, calculated as the wavelength

202   position of the minimum of a fourth-order polynomial fit to the spectrum within 0.1 µm

203   of the minimum channel in each band. Band depth is the percent depth below the

204   continuum at the location of the band center (*i.e*., one minus the value of the continuum

205   removed spectrum at that wavelength). The 1 and 2 µm band positions together can be

206   used to broadly distinguish between orthopyroxene (OPX; band centers between 0.9-0.94

207   and 1.8-1.95 µm), clinopyroxene (CPX; 0.98-1.06 and 2.05-2.4 µm), and iron-bearing

208   glass (1.06-1.2 and 1.9-2.05 µm). Mixtures of these minerals have band centers that fall

209   in the intermediate regions between the endmembers (Horgan et al., 2014). Other iron-

210   bearing minerals can also be identified using similar methods. Olivine exhibits a

211   characteristically asymmetric 1 µm band typically centered near 1.05-1.08 µm and

212   plagioclase feldspars exhibit broad and shallow bands centered between 1.25-1.35 µm,

213   but neither exhibits a corresponding 2 µm band.

214   Once band parameters are calculated, the resulting parameter images are mapped

215   into a mosaic with a local cylindrical projection at 140 m/pixel horizontal resolution

216   (Figure 3).

217

218

219 **Supplemental Table DR3:** M^3 images used to construct mosaic shown in Figures 3 and

220 Supplemental Figure DR5.

Product ID	Observation Time	Center Latitude (°N)	Center Longitude (°E)
M3G20090424T010115_V01_RFL	2009-04-24T01:23:31.000	-23.045	241.168
M3G20090424T031100_V01_RFL	2009-04-24T03:34:29.000	16.468	240.198
M3G20090424T050542_V01_RFL	2009-04-24T05:25:20.000	-5.585	238.938
M3G20090424T070715_V01_RFL	2009-04-24T07:30:44.000	16.945	238.105
M3G20090424T085330_V01_RFL	2009-04-24T09:17:14.500	-18.333	237.05
M3G20090424T191252_V01_RFL	2009-04-24T19:27:00.000	41.377	231.182
M3G20090424T204145_V01_RFL	2009-04-24T20:50:11.000	-65.399	230.521
M3G20090424T205837_V01_RFL	2009-04-24T21:13:55.500	7.295	230.199
M3G20090424T225130_V01_RFL	2009-04-24T23:07:19.000	-6.977	229.293
M3G20090425T024715_V01_RFL	2009-04-25T02:57:57.500	-23.702	227.212
M3G20090425T043400_V01_RFL	2009-04-25T04:43:54.500	-60.745	226.512
M3G20090425T045349_V01_RFL	2009-04-25T05:08:01.000	13.112	225.975
M3G20090425T064315_V01_RFL	2009-04-25T06:58:15.500	-10.814	225.073
M3G20090425T083000_V01_RFL	2009-04-25T08:42:57.000	-51.704	224.421
M3G20090425T202308_V01_RFL	2009-04-25T20:44:48.000	-9.985	217.877
M3G20090425T222745_V01_RFL	2009-04-25T22:50:47.000	14.306	216.639
M3G20090426T001430_V01_RFL	2009-04-26T00:35:15.500	-27.142	215.83
M3G20090426T041030_V01_RFL	2009-04-26T04:34:37.000	-17.046	213.824
M3G20090426T061945_V01_RFL	2009-04-26T06:43:36.500	16.539	212.169
M3G20090426T080645_V01_RFL	2009-04-26T08:24:01.500	-37.386	211.727
M3G20090426T120245_V01_RFL	2009-04-26T12:20:36.500	-35.643	209.331
M3G20090426T141200_V01_RFL	2009-04-26T14:17:39.500	-38.692	208.292
M3G20090426T142319_V01_RFL	2009-04-26T14:41:23.500	34.043	207.238
M3G20090426T160558_V01_RFL	2009-04-26T16:19:53.000	-25.757	207.043
M3G20090426T180800_V01_RFL	2009-04-26T18:15:02.500	-34.483	206.076
M3G20090426T182205_V01_RFL	2009-04-26T18:32:56.000	20.317	205.061
M3G20090426T195445_V01_RFL	2009-04-26T20:06:44.000	-53.767	206.102
M3G20090426T235045_V01_RFL	2009-04-27T00:01:18.000	-58.136	203.834
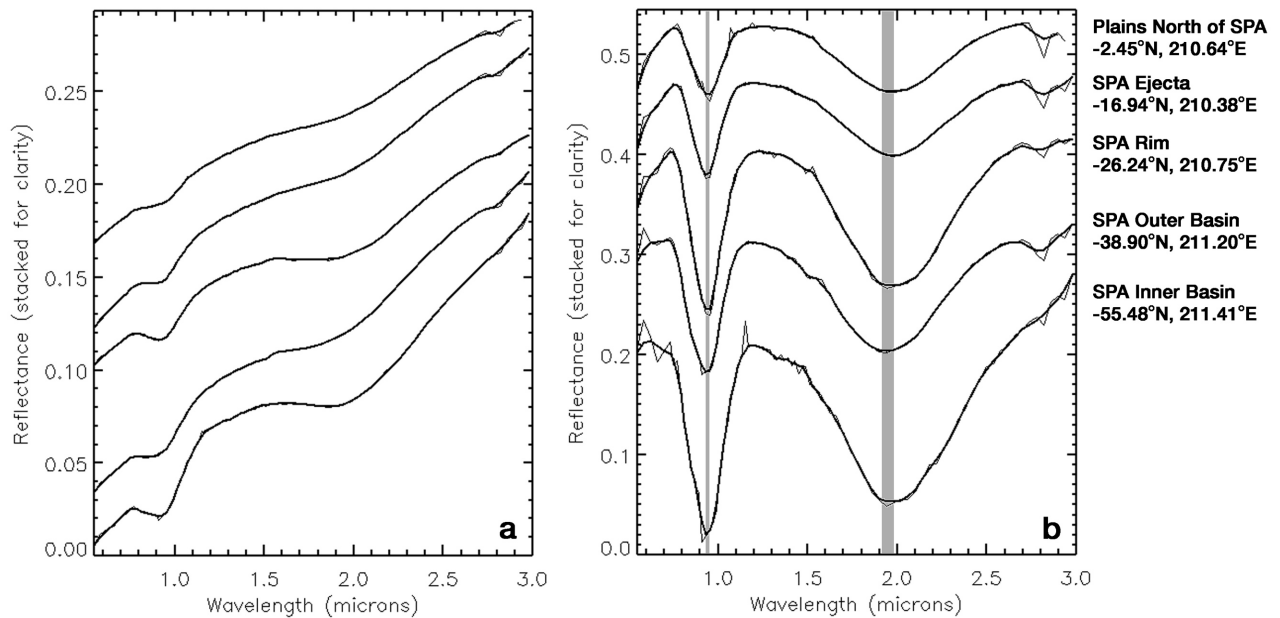
Supplemental Figure DR5: (a) Reflectance and (b) continuum removed spectra of LCP-dominated regions at locations indicated by lat/long coordinates, and by stars in Figure 3a. Grey bars indicate the range of ~1 and ~2 μm band centers for these spectra, which are consistent with LCP.

REFERENCES:

Adams, J.B., 1974, Visible and near-infrared diffuse reflectance spectra of pyroxenes as applied to remote sensing of solid objects in the solar system: Journal of Geophysical Research,, p. 1–8.

Bennett, K.A., Horgan, B.H.N., Gaddis, L.R., Greenhagen, B.T., Allen, C.C., Hayne, P.O., Bell, J.F., III, and Paige, D.A., 2016, Complex explosive volcanic activity on the Moon within Oppenheimer crater: Icarus, v. 273, p. 1–19, doi: 10.1016/j.icarus.2016.02.007.

Benz, W., Cameron, A., and Melosh, H.J., 1989, The origin of the Moon and the single-impact hypothesis III: Icarus, v. 81, p. 113–131.

Besse, S., Sunshine, J., Staid, M., Boardman, J., Pieters, C., Guasqui, P., Malaret, E., McLaughlin, S., Yokota, Y., and Li, J.-Y., 2013, A visible and near-infrared photometric correction for Moon Mineralogy Mapper (M3): Icarus, v. 222, p. 229–242, doi: 10.1016/j.icarus.2012.10.036.

Boardman, J.W., Pieters, C.M., Green, R.O., Lundeen, S.R., Varanasi, P., Nettles, J., Petro, N., Isaacson, P., Besse, S., and Taylor, L.A., 2011, Measuring moonlight: An

245 overview of the spatial properties, lunar coverage, selenolocation, and related Level
246 1B products of the Moon Mineralogy Mapper: J. Geophys. Res, v. 116, p. 65–15,
247 doi: 10.1029/2010JE003730.

248 Clark, R.N., Pieters, C.M., Green, R.O., Boardman, J.W., and Petro, N.E., 2011, Thermal
249 removal from near-infrared imaging spectroscopy data of the Moon: J. Geophys. Res,
250 v. 116, p. E00G14–9, doi: 10.1029/2010JE003751.

251 Cloutis, E.A., and Gaffey, M.J., 1991, Spectral-compositional variations in the
252 constituent minerals of mafic and ultramafic assemblages and remote sensing
253 implications: Earth, v. 53, p. 11–53, doi: 10.1007/BF00116217.

254 Collins, G.S., Melosh, H.J., and IVANOV, B.A., 2004, Modeling damage and
255 deformation in impact simulations: Meteoritics and Planetary Science, v. 39, p. 217–
256 231, doi: 10.1111/j.1945-5100.2004.tb00337.x.

257 Cushing, J. A., Taylor, G. J., Norman, M. D. & Keil, K. The granulitic impactite suite:
258 Impact melts and metamorphic breccias of the early lunar crust. *Meteoritics
259 & Planetary Science* **34,** 185–195 (1999).
260
261 Hudgins, J. A., Spray, J. G. & Hawkes, C. D. Element diffusion rates in lunar granulitic
262 breccias: Evidence for contact metamorphism on the Moon. *American Mineralogist*
263 **96,** 1673–1685 (2011).2011.

264 Elbeshausen, D., and Wünnemann, K., 2011, iSALE-3D: A three-dimensional, multi-
265 material, multi-rheology hydrocode and its applications to large-scale geodynamic
266 processes, *in* Schäfer, F. and Hiermaier, S. eds., Proceedings of 11th Hypervelocity
267 Impact Symposium (HVIS), Stuttgart, Fraunhofer Verlag, p. 287–301.

268 Elbeshausen, D., Wünnemann, K., and Collins, G.S., 2009, Scaling of oblique impacts in
269 frictional targets: Implications for crater size and formation mechanisms: Icarus, v.
270 204, p. 716–731, doi: 10.1016/j.icarus.2009.07.018.

271 Garrick-Bethell, I., and Zuber, M.T., 2009, Elliptical structure of the lunar South Pole-
272 Aitken basin: Icarus, v. 204, p. 399–408, doi: 10.1016/j.icarus.2009.05.032.

273 Green, R.O., Pieters, C., Mouroulis, P., Eastwood, M., Boardman, J., Glavich, T.,
274 Isaacson, P., Annadurai, M., Besse, S., Barr, D., Buratti, B., Cate, D., Chatterjee, A.,
275 Clark, R., et al., 2011, The Moon Mineralogy Mapper (M 3) imaging spectrometer
276 for lunar science: Instrument description, calibration, on-orbit measurements, science
277 data calibration and on-orbit validation: J. Geophys. Res, v. 116, p. 367–31, doi:
278 10.1029/2011JE003797.

279 Hicks, M.D., Buratti, B.J., Nettles, J., Staid, M., Sunshine, J., Pieters, C.M., Besse, S.,
280 and Boardman, J., 2011, A photometric function for analysis of lunar images in the
281 visual and infrared based on Moon Mineralogy Mapper observations: J. Geophys.
282 Res, v. 116, p. 392–10, doi: 10.1029/2010JE003733.

283 Hirt, C.W., Amsden, A.A., and cook, J.L., 1974, An arbitrary Lagrangian-Eulerian
284   comuting method for all flow speeds: Journal of Computataional Physics, v. 14, p.
285   227–253.

286 Horgan, B.H.N., Cloutis, E.A., Mann, P., and Bell, J.F., III, 2014, Near-infrared spectra
287   of ferrous mineral mixtures and methods for their identification in planetary surface
288   spectra: Icarus, v. 234, p. 132–154, doi: 10.1016/j.icarus.2014.02.031.

289 Johnson, G.R., and Cook, W.H., 1983, A constitutive model and data for metals subjected
290   to large strains, high strain rates and high temperatures, *in* v. 21.

291 Laneuville, M., Wieczorek, M.A., Breuer, D., and Tosi, N., 2013, Asymmetric thermal
292   evolution of the Moon: Journal of Geophysical Research: Planets, v. 118, p. 1435–
293   1452, doi: 10.1002/jgre.20103.

294 Marsh, S. P., 1980, LASL Shock Hugoniot Data, Berkeley, University of California Press,
295   658 p.

296 Melosh, H.J., 1989, Impact Cratering: A Geologic Process: New York, Oxford University
297   Press, 245 p.

298 Ohnaka, M., 1995, A shear failure strength law of rock in the brittle-plastic transition
299   regime: Geophys. Res. Lett, v. 22, p. 25–28.

300 Pierazzo, E., Artemieva, N., Asphaug, E., Baldwin, E.C., Cazamias, J., Coker, R., Collins,
301   G.S., Crawford, D.A., Davison, T., Elbeshausen, D., Holsapple, K.A., Housen, K.R.,
302   Korycansky, D.G., and Wünnemann, K., 2008, Validation of numerical codes for
303   impact and explosion cratering: Impacts on strengthless and metal targets:
304   Meteoritics and Planetary Science, v. 43, p. 1917–1938, doi: 10.1111/j.1945-
305   5100.2008.tb00653.x.

306 Pierazzo, E., Vickery, A.M., and Melosh, H.J., 1997, A reevaluation of impact melt
307   production: Icarus, v. 127, p. 408–423, doi: 10.1006/icar.1997.5713.

308 Pieters, C.M., Boardman, J., Buratti, B., and Chatterjee, A., 2009, The Moon Mineralogy
309   Mapper (M3) on Chandrayaan-1: Curr Sci.

310 Potter, R.W.K., Collins, G.S., Kiefer, W.S., McGovern, P.J., and Kring, D.A., 2012,
311   Constraining the size of the South Pole-Aitken basin impact: Icarus, v. 220, p. 730–
312   743, doi: 10.1016/j.icarus.2012.05.032.

313 Sunshine, J.M., and Pieters, C.M., 1993, Estimating Modal Abundances From the Spectra
314   of Natural and Laboratory Pyroxene Mixtures Using the Modified Gaussian Model:
315   Journal of Geophysical Research (ISSN 0148-0227), v. 98, p. 9075–9087, doi:
316   10.1029/93JE00677.

317 Thompson, S.L., 1990, ANEOS: Analytic equations of state for shock physics codes
318   input manual: Sandia National Laboratories.

319 Wieczorek, M.A., Neumann, G.A., Nimmo, F., Kiefer, W.S., Taylor, G.J., Melosh, H.J.,
320   Phillips, R.J., Solomon, S.C., Andrews-Hanna, J.C., Asmar, S.W., Konopliv, A.S.,
321   Lemoine, F.G., Smith, D., Watkins, M.M., et al., 2013, The Crust of the Moon as
322   Seen by GRAIL: Science, v. 339, p. 671–675, doi: 10.1126/science.1231530.

323 Wünnemann, K., Collins, G.S., and Melosh, H.J., 2006, A strain-based porosity model
324   for use in hydrocode simulations of impacts and implications for transient crater
325   growth in porous targets: Icarus, v. 180, p. 514–527, doi:
326   10.1016/j.icarus.2005.10.013.

327